Thesis for the degree of Licentiate of Philosophy

Investigating hydrothermal stability and influence of water on the activity of Cu-CHA catalysts for NH_3-SCR

Shivangi Singh

Department of Physics
Chalmers University of Technology
Göteborg, Sweden 2024

Investigating hydrothermal stability and influence of water on the activity of Cu-CHA catalysts for NH_3-SCR
Shivangi Singh

© Shivangi Singh, 2024

Thesis for the degree of Licentiate of Philosophy 2024

Department of Physics
Chalmers University of Technology
SE-412 96 Göteborg
Sweden
Telephone: +46 (0)31-772 1000

Printed at Chalmers Digitaltryck
Göteborg, Sweden 2024

Investigating hydrothermal stability and influence of water on the activity of Cu-CHA catalysts for NH_3-SCR

Shivangi Singh
Department of Physics
Chalmers University of Technology

Abstract

Selective catalytic reduction of nitrogen oxides (NO_x) with NH_3 as a reducing agent (NH_3- SCR) is a leading technology for diesel exhaust emission control. Cu-exchanged zeolites with the chabazite structure (Cu-CHA) have emerged as the preferred catalysts thanks to its high activity and hydrothermal stability. Hydrothermal stability is related to dealumination, i.e. removal of aluminum from the zeolite framework to form extra-framework aluminum, at high temperatures in the presence of water vapor. Copper-exchanged chabazite (Cu-CHA) zeolites have higher hydrothermal stability compared to H-chabazite (H-CHA).

To understand the delayed dealumination of Cu-CHA catalysts, we have investigated the reaction paths for dealumination in H-CHA and Cu-CHA using density functional theory (DFT) calculations combined with microkinetic modeling. We find that Cu-CHA and H-CHA follow similar four-step hydrolysis processes, yet the dealumination of Cu-CHA has higher energy barriers, suggesting stabilization of the CHA structure by Cu ions. Furthermore, the preferred reaction product upon complete dealumination of Cu-CHA is a copper-aluminate like species bound to the zeolite framework. The microkinetic analysis quantifies the increased stability of Cu-CHA as compared to H-CHA.

In addition to the high-temperature dealumination, we investigated the role of water on low-temperature SCR by experimentally measuring the activity and reaction order of water. The reaction order of water is found to be increasingly negative with increasing water pressure. DFT calculations reveal that water blocks the active Cu-sites and a DFT-based microkinetic model reproduces the measured change of reaction order with water pressure.

Keywords: Catalysis, Density Functional Theory, Microkinetic modeling, Cu-CHA, Ammonia assisted selective catalytic reduction

List of Publications

This thesis is based on the following appended papers:

I. Mechanism for Cu-enhanced hydrothermal stability of Cu-CHA for NH_3-SCR
S. Singh, T.V.W. Janssens, and H. Grönbeck
Catalysis Science & Technology (In revision)

II. Effect of water on the low-temperature NH_3-SCR rate over Cu-CHA.
S. Singh, Y. Feng, T.V.W. Janssens, and H. Grönbeck
In manuscript

My contributions to the publications

Paper I
I performed all the DFT calculations and kinetic simulations. I wrote the first draft of the paper, which was finalized together with my coauthors.

Paper II
I performed all the experiments and DFT calculations. I wrote the first draft of the corresponding parts in the manuscript.

Contents

Chapter 1

Introduction

Transportation serves as the essential lifeline for both people and goods in society, yet it significantly contributes to air pollution and climate change through emissions.[1] In addition to CO_2, which is a greenhouse gas, the emissions from transportation contain pollutants such as unburned hydrocarbons, carbon monoxide (CO), sulfur oxides (SO_x), and nitrogen oxides (NO_x).[2] NO_x emissions have detrimental environmental effects, including acid rain, urban smog, and respiratory health problems, underscoring stringent emission standards and development of the technologies for emission control.[3]

For gasoline engines, which operate with an air/fuel ratio close to stoichiometry, the three-way catalyst (TWC) has proven effective.[4] The TWC converts (NO_x), unburned hydrocarbons, and CO into nitrogen (N_2), carbon dioxide (CO_2), and water (H_2O). The typical TWC includes precious metals such as platinum (Pt) and palladium (Pd) supported on alumina (Al_2O_3) and uses ceria (CeO_2) or ceria-based materials as promoters thanks to their oxygen storage capacity. However, the TWC is not suitable for controlling emissions from diesel engines, which operate under lean conditions with excess oxygen.[4]

Selective catalytic reduction (SCR) has emerged as an efficient solution to control the NO_x emissions from diesel engines. SCR reduces NO_x emissions by using a reducing agent, commonly ammonia (NH_3), which reacts with NO_x over a catalyst to produce nitrogen and water.[5] This technology is crucial for mitigating the harmful effects of NO_x and has become widely adopted for its efficiency, thus playing an essential role in environmental protection.

1.1 Heterogeneous catalysis

Catalysis is essential in both natural and industrial settings.[6] Enzymes act as nature's catalysts, while synthetic catalysts are used to synthesize chemicals, produce fuels, and control emissions. Figure 1.1 shows a free energy diagram for a catalyzed reaction. Catalysis is a fundamental process in chemistry where a substance (catalyst) speeds up a chemical reaction without being consumed in the process. Catalysts lower the activation energy of the reaction and create an alternative pathway for the reaction. Consequently, both the forward and reverse reactions proceed at a faster rate and to the same extent in the presence of a catalyst which accelerates the approach to equilibrium.[6;7] However, the equilibrium constant remains unchanged as the catalyst does not affect the thermodynamics of the initial and final states of the catalyst. Thus, if a reaction is thermodynamically unfavorable, a catalyst does not change this situation. A catalyst changes the kinetics but not the thermodynamics. The catalyst can be divided into three categories: homogeneous catalyst, enzymatic catalyst, and heterogeneous catalyst.[8]

Homogeneous catalysts operate within the same phase as the reactants, typically

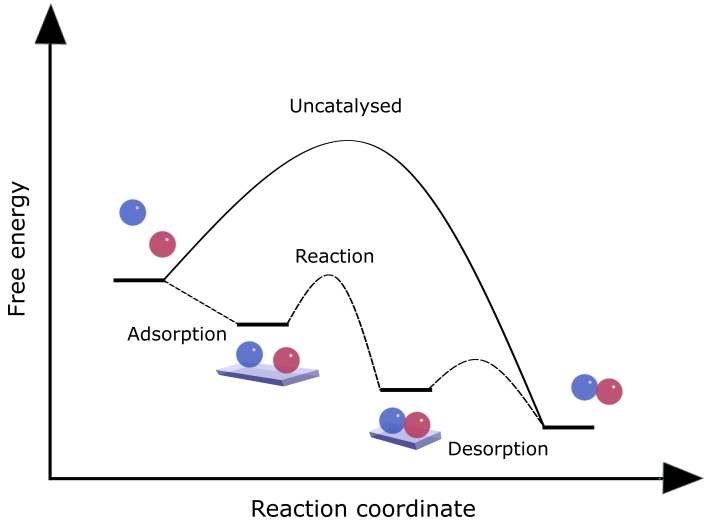

Figure 1.1: Sketch of the free energy diagram for an uncatalyzed reaction and a catalyzed reached (dotted lines).

as dissolved species in the reaction mixture, often involving coordination complexes or organometallic compounds. Enzymatic catalysts, on the other hand, are specialized biological molecules that accelerate biochemical reactions. In contrast, heterogeneous catalysts have a different phase from the reactants. An important example of a heterogeneous catalytic reaction is the Haber-Bosch process in which ammonia is synthesized from hydrogen and nitrogen.[6] Another example of a heterogeneous catalytic reaction is the selective catalytic reduction (SCR) reaction studied in this thesis in which NO_x is reduced to N_2 and H_2O with NH_3 as a reducing agent. The reactants and products are in the gas phase, while the catalyst is usually a solid material, such as a metal oxides or zeolites. In this thesis, the focus is on ammonia-assisted SCR using copper-based zeolites.

1.2 Ammonia assisted selective catalytic reduction

Ammonia-assisted Selective Catalytic Reduction (SCR) is a process where ammonia (NH_3) selectively reacts with nitrogen oxides NO_x in the presence of a catalyst to produce nitrogen (N_2) and water (H_2O). One feature of SCR is the use of ammonia as a reducing agent, which specifically targets NO_x for reduction. Experiments with isotopically labeled reactants show that N_2 takes one nitrogen atom from a molecule of NO_x and the other nitrogen from ammonia.[9]

In diesel engine emissions, NO_x primarily consists of nitric oxide (NO) with a smaller proportion of nitrogen dioxide (NO_2). The NH_3-SCR process can be categorized based on the predominance of NO or NO_2.The overall reaction for the so-called, standard SCR reaction, where NH_3 reduces NO is given by:[10]

$$4NH_3 + 4NO + O_2 \rightarrow 4N_2 + 6H_2O \tag{1.1}$$

The NO:NH_3 stoichiometry of the reaction is one and O_2 is needed to accommodate the hydrogen atoms.

When NO and NO_2 are in 1:1, the overall reaction is given by the so-called, fast-SCR reaction:

$$4NH_3 + 2NO + 2NO_2 \rightarrow 4N_2 + 6H_2O \tag{1.2}$$

The fast-SCR reaction does not need O_2 and is generally more facile than the standard SCR reaction. If the ratio of NO to NO_2 is below 0.5, the SCR reaction is driven primarily by NO_2 with the overall reaction:

$$8NH_3 + 6NO_2 \rightarrow 7N_2 + 12H_2O \tag{1.3}$$

This reaction has NH_3:NO stoichiometry that is higher than 1 and should therefore be avoided. Reactions (1.1) and (1.2) are preferable outcomes of the NH_3-SCR reaction. However, there is the possibility of unselective reactions, such as the oxidation of NH_3 which produces NO_x instead of reducing it or formation of N_2O which is a potential greenhouse gas, which are given by the following:[11]

$$4NH_3 + 3O_2 \rightarrow 2N_2 + 6H_2O \tag{1.4}$$

$$4NH_3 + 5O_2 \rightarrow 4NO + 6H_2O \tag{1.5}$$

$$2NH_3 + 2O_2 \rightarrow N_2O + 3H_2O \tag{1.6}$$

$$2NH_3 + 2NO_2 \rightarrow N_2O + N_2 + 3H_2O \tag{1.7}$$

$$6NH_3 + 8NO_2 \rightarrow 7N_2O + 9H_2O \tag{1.8}$$

1.3 Catalysts for NH_3-SCR

An ideal catalyst for selective catalytic reduction in diesel exhaust is one that exhibits high activity at low temperatures, with the typical temperature for highway driving conditions being around 200°C.[12] The catalyst must possess redox abilities to effectively facilitate oxygen adsorption and dissociation, crucial for the SCR reactions. The catalyst should also adsorb NO and NH_3 to promote their coupling to form nitrogen before complete dissociation of NH_3. This will minimize unwanted reactions that produce byproducts (equation 1.4 to 1.8). Additionally, it should be resistant to poisoning by sulfur and hydrothermal aging. A variety of catalysts have been used over the years including including noble metals,[13] transition metal oxides,[14;15] and zeolite.[16;17]

1.3.1 V_2O_5-based catalysts

Vanadium-based catalysts, specifically V_2O_5 supported on TiO_2 with WO_3 as a promoter, are utilized in stationary commercial SCR processes thanks to their high NO_x removal activity.[18] Vanadia serves as the primary active site for NO removal, with WO_3 acting as a promoter for the reaction.[19] Vanadia SCR catalysts exhibit an optimal NO_x conversion range, peaking between approximately 250°C and 500°C.[20] At temperatures below 250°C, the reaction between NO and NH_3 is slow, resulting in decreased NO_x conversion. Conversely, at temperatures exceeding roughly 450-500°C, the SCR efficiency declines due to the preferential oxidation of NH_3 by O_2 rather than its reaction with NO. However, also in the active temperature interval, these catalysts have drawbacks.[18] They can generate toxic volatile vanadia species and are sensitive to poisoning by sulfur, as TiO_2 can be weakly and reversibly sulfated under SCR reaction conditions.[21]

1.3.2 Metal-exchanged zeolite catalysts

Zeolites are alumino-silicates, with tetrahedral units of SiO_4 and AlO_4.[22] The tetrahedral units form rings of different size, which make up the porous zeolite structure. The substitution of Si by Al in the structure introduces a negative charge, which is balanced by protons, creating Brønsted acidity.[23] This acidity plays a crucial role in zeolites catalytic properties, as these protons can be exchanged with metal cations like Na, K, Fe, and Cu. Such metal-exchanged zeolites exhibit Lewis acidity, enhancing their catalytic performance in various reactions.[24;25]

Copper and iron-exchanged zeolites have shown exceptional success in NH_3-SCR activities due to their excellent redox properties.[25] They offer a broader operational temperature range and greater resistance to sulfur poisoning compared to vanadium-based catalysts.[26] For instance, Cu-exchanged zeolites excel in NO_x reduction at temperatures below 350 °C. Iron-exchanged zeolites have a higher activity at high temperatures, highlighting the significance of metal type for the metal-exchanged zeolite performance.[27]

Various copper-exchanged zeolites such as Cu-ZSM-5, Cu-BEA, and Cu-CHA have been explored for NH_3-SCR reactions.[28] ZSM-5, BEA and CHA zeolites are characterized by their distinct pore sizes and ring structures, making them suitable for varied applications. ZSM-5 has medium pore openings of about 5.5 to 5.6 Ångstroms with ten-membered rings as its largest. BEA zeolite features larger pores around 7.6 Ångstroms with the largest ring consisting of 12 Si atoms. CHA, or Chabazite, as shown in Figure 1.2 has smaller pore openings of approximately 3.8 Ångstroms with four, six, and eight-membered rings.[26] Among the different zeolites, Cu-CHA stands out for its superior activity and selectivity for N_2 formation[29].

1.4 Hydrothermal aging of zeolites

One general issue with zeolite-based catalysts is deactivation due to dealumination when the catalyst material is exposed to water vapor at high temperatures (>850 K for Cu-CHA[30]). Dealumination refers to the removal of aluminum from the zeolite framework, resulting in structural changes that adversely affect the catalytic activity, leading to

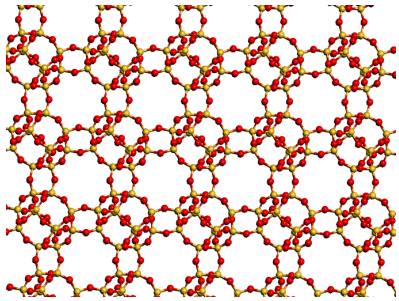

Figure 1.2: Ball and stick model of the CHA structure. Atomic color code: aluminum (purple), silicon (yellow), and oxygen (red).

catalyst degradation.[31;32] In dealumination, sequential breakage of the Al-O bonds takes place which ultimately results in the formation of silanol groups and extra-framework Al.[33;34] The scheme for sequential hydrolysis is shown in Figure 1.3.

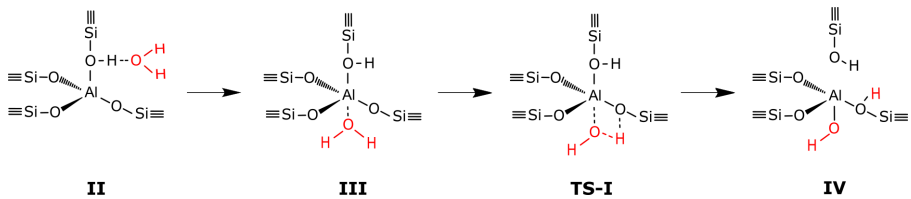

Figure 1.3: Reaction scheme for hydrolysis of the first Al-O bond in H-CHA.

It is known that the hydrothermal stability of Cu-CHA is higher than that of H-CHA, which means that H-CHA experiences more dealumination than Cu-CHA under similar conditions.[35] This can be shown with infrared spectroscopy and temperature-programmed desorption in which dealumination is associated with a decrease in the number of brønsted acid sites. Early XRD measurements show that the zeolite structure of NH_4-CHA breaks down at 850-900 K, whereas Cu-CHA remains stable up to 1100-1150 K.[36] Furthermore, studies varying Cu loading and the Si/Al ratio have revealed that high Cu loading decreases hydrothermal stability compared to moderate loading,[35] and that a more severe degradation is observed with increasing Si/Al ratio.[37]

1.5 Objective

The objective of this thesis is to investigate the effect of water on the zeolite framework in H-CHA and Cu-CHA at high temperatures and the effect of water on the SCR reaction at low temperatures.

In **Paper I**, dealumination mechanism in H-CHA and Cu-CHA is explored using density functional theory (DFT) calculations. It was found the formation of mobile $Al(OH)_3H_2O$ in Cu-CHA is associated with a high energy barrier and the preferred reaction product after complete dealumination of Cu-CHA is a Cu-Aluminate-like species

bound to the zeolite framework. Furthermore, to study the kinetics of the reaction a microkinetic model was constructed based on energy landscapes and it was found that dealumination in Cu-CHA is a much slower process compared to H-CHA. In addition to this, the effect of Al-distribution on dealumination was also studied.

In **Paper II**, the impact of water on NH_3-SCR over Cu-CHA catalysts is investigated using a combination of experimental studies, density functional theory (DFT) calculations, and microkinetic modeling. The study reveals that water exhibits inhibitory effects on the NH_3-SCR process below 260°C and across water partial pressures ranging from 2% to 20%. Experimental determination of reaction orders revealed that the negative reaction order increases linearly from 0 in the absence of H_2O to -1.4 at 20% H_2O. Additionally, DFT calculations demonstrate competitive adsorption of water molecules on different Cu species, influencing the reaction cycle. A DFT-based microkinetic model, considering active site blocking by water, is developed, showing good agreement with the experimentally observed changes in reaction order with respect to water pressure.

Chapter 2

Electronic structure calculations

Electronic structure calculations play a crucial role in understanding material properties at a fundamental level. In catalysis, electronic structure calculations are used to explore bond strengths, structures, and reaction mechanisms. The electronic structure is obtained by solving the Schrödinger equation, which has long posed challenges in terms of finding solutions. To address this issue, there has been a progression from Hartree-Fock approximations to the more advanced Density Functional Theory (DFT). This chapter focuses on electronic structure calculations, with an emphasis on Density Functional Theory (DFT).

2.1 The Schrödinger equation

The time-independent, non-relativistic Schrödinger equation is given by [38]:

$$\hat{H}\Psi = E\Psi \tag{2.1}$$

where $\hat{H}$, Ψ and E are the Hamiltonian energy operator, wave function, and the total energy of the system, respectively. The total wavefunction Ψ contains all the information and properties of the system and is fundamental in a quantum mechanical description. However, the real physical interpretation of Ψ lies when it is squared as $|\Psi|^2$ which can be interpreted as the probability density of finding a particle described by the wave function Ψ.

The Schrödinger equation is highly complex and solvable only for hydrogen-like systems. The Born-Oppenheimer approximation is generally the first approximation when solving the Schrödinger equation. [39] The nuclei, being much more massive than electrons (1840 times the mass of a hydrogen nucleus), lead electrons to quickly occupy the ground state configuration whenever a nucleus moves. This assumption allows us to consider the position of nuclei as fixed and consider the total wavefunction as the product of the wavefunction for the electrons and the wavefunction for the nucleus.

The Hamiltonian operator,$\hat{H}$ in equation 2.1, is a sum of the kinetic and potential operators involved.

$$\hat{H} = E_I^{\text{kin}} + E_i^{\text{kin}} + U_{Ii} + U_{ij} + U_{IJ} \tag{2.2}$$

where, E_I^{kin} and E_i^{kin} are the kinetic energy operators of the nuclei and electrons, respectively. U_{Ii}, U_{ij}, U_{IJ} are the potential energy operators describing the Coulomb interactions between nucleus–electron, electron-electron, and nucleus–nucleus, respectively. As a result of the Born-Oppenheimer approximation, the Hamiltonian for the electrons is described as:

$$\hat{H}_e = E_i^{\text{kin}} + U_{Ii} + U_{ij} \tag{2.3}$$

2.2 Early first-principles calculations

The Schrödinger equation is solvable only for single-electron systems. To tackle many-body problems, approximations are employed. Hartree's approach simplifies this by treating each electron independently, representing interactions with others via an average electron density instead of individual interactions.[40] This transforms the complex n-electron system into a set of non-interacting one-electron systems influenced by a collective average field.

$$\left(-\frac{1}{2}\nabla^2 + U_{\text{ext}}(\mathbf{r}) + U_H(\mathbf{r})\right)\Psi_e(\mathbf{r}) = E\Psi_e(\mathbf{r}) \tag{2.4}$$

where, U_{ext} is the attractive interaction between electrons and nuclei, U_H is the Hartree potential coming from the classical Coulomb repulsive interaction between each electron and the mean field. Here, the Hamiltonian is expressed in atomic units (a.u.), which form a system of natural units that is particularly convenient for atomic-scale calculations. The N-electron wave function can be simply approximated as the product of N numbers of one-electron wave functions:

$$\Psi_e = \psi_1 \times \psi_2 \times \cdots \times \psi_n N \tag{2.5}$$

In the Hartree-Fock method,[41] the N-electron wavefunction is approximated as a linear combination of non-interacting one-electron wave functions arranged in the form of a Slater determinant. This wavefunction follows the antisymmetry principle, ensuring that the wave function changes sign when the coordinates of any two electrons are exchanged, reflecting the fermionic nature of electrons, which was neglected in the Hartree method. The Hartree-Fock approach seeks to find the set of wave functions that minimizes the total energy of the system by iteratively solving the Schrödinger equation. However, the Hartree-Fock method fails to accurately describe systems with pronounced electron correlation which leads to inaccuracies in describing the chemical bonds.

2.3 The density functional theory

The concept of working with electron density rather than wavefunctions originated in 1927 when Thomas and Fermi independently introduced the idea.[42;43] However, the formal verification awaited Hohenberg and Kohn's two theorems in 1964. The first theorem asserts that a unique external potential U_{ext} is solely determined by the ground-state electron density, implying that the energy can be expressed as a functional of the electron density. Consequently, the external potential determines the system's Hamiltonian, and the Hamiltonian dictates all properties of the system, it follows that the ground-state electron density effectively governs all ground state system properties, including the ground-state wavefunction.[44]

The second theorem by Hohenberg and Kohn proves that the ground state of a system can be determined using the variational principle. The electron density giving the lowest energy value represents the true ground-state electron density, which can subsequently be utilized to compute various system properties.[44]

Later, Kohn and Sham proposed an approach to evaluate the density functional.[45] In the Kohn-Sham approach, electrons are initially assumed to be non-interacting, following

the mapping of the interacting N-electron system onto a non-interacting one-electron system under the given external potential. This fictitious system of non-interacting electrons effectively captures the essential electronic structure of the original many-body system.[45] The energy functional in the Kohn-Sham approach is defined by:

$$E_{\mathrm{KS}} = T_0[n(\mathbf{r})] + \int n(\mathbf{r}) V_{\mathrm{ext}}(\mathbf{r})\, dr + E_H[n(\mathbf{r})] + E_{xc}[n(\mathbf{r})]. \tag{2.6}$$

Here, n($\mathbf{r}$) is the electron density, the first term is the kinetic energy of the non-interacting electrons, and the second term comes from the interaction between the electrons and the external potential. The third term (Hartree energy) arises from the interaction between an electron and the mean electron density in a mean-field approximation. The last term is the exchange-correlation energy, which also includes the kinetic energy resulting from the interactions between the electrons. This will be discussed in next section. By applying the variational principle on the Kohn-Sham energy functional

$$\frac{\delta E_{\mathrm{KS}}}{\delta \psi_i^*(\mathbf{r})} = 0, \tag{2.7}$$

it is possible to derive the Kohn-Sham equation for an electron i with single electron wavefunction ψ_i

$$-\frac{1}{2}\nabla^2 \psi_i(\mathbf{r}) + \left[V_{\mathrm{ext}}(\mathbf{r}) + \int \frac{n(\mathbf{r}')}{|\mathbf{r} - \mathbf{r}'|}\, d\mathbf{r}' + \frac{\delta E_{xc}}{\delta n(\mathbf{r})} \right] \psi_i(\mathbf{r}) = \epsilon_i \psi_i(\mathbf{r}). \tag{2.8}$$

This reformulation and treatment of independent electrons will provide a much easier and more effective way of calculation. Over the years, it has been demonstrated that this approach closely mimics the true ground-state density, enabling the description of chemical bonds with reasonable accuracy.

2.3.1 Approximations to the exchange-correlation functional

The exchange-correlation part of the energy functional plays a crucial role as it captures many-body quantum mechanical effects.[46] The exchange energy term originates from the quantum mechanical exchange interaction, reflecting the antisymmetry of the electron wavefunction. This term quantifies the energy associated with the exchange of electrons with the same spin, meaning that two electrons cannot occupy the same quantum state. The correlation energy term accounts for the correlated motion of electrons.[47]

Local density approximation

The Local Density Approximation (LDA) is a simple the estimation of the exchange-correlation (xc) energy in many-electron systems. It assumes a locally uniform electron density, allowing the calculation of xc- energy based on the properties of a homogeneous electron gas. This approach treats complex systems as composed of small, uniform pieces with constant electron density.[45] The exchange and correlation energies per electron in a homogeneous electron gas can be accurately calculated using quantum Monte Carlo simulations and represented analytically[48]:

$$E_{xc}^{\mathrm{LDA}}[n(\mathbf{r})] = \int \epsilon_{xc}^{\mathrm{hom}}[n(\mathbf{r})]n(\mathbf{r})\, d\mathbf{r}, \tag{2.9}$$

LDA proves effective for calculating the lattice parameters for various materials, particularly those with slowly changing electron density like 3d metals. Nevertheless, LDA tends to over-predict the cohesive energies, by as much as 1 to 2 eV, and falls short in representing systems with rapidly varying electron density and strong correlations.

Generalized gradient approximation

The Generalized Gradient Approximation (GGA) represents an improvement over the Local Density Approximation (LDA). GGA incorporates both local and semi-local information by considering the electron density and its gradient at a specific point .[49;50] The general form of GGA in practice is expressed based on the LDA with an additional enhancement factor F(s) that directly modifies the LDA energy:

$$E_{xc}^{GGA}[n(r), s] = \int \epsilon_{xc}^{LDA}[n(r)]n(r)F(s)\, dr \tag{2.10}$$

$$s = C\frac{|\nabla n(r)|}{n^{4/3}(r)} \tag{2.11}$$

Here, s is defined as a dimensionless quantity that depends on the electron density $n(\mathbf{r})$ and its gradient $\nabla n(\mathbf{r})$, scaled by a constant C. GGA addresses some of LDA's limitations by considering the inhomogeneities in electron density distribution. This leads to more accurate predictions of structural properties, reaction energies, and molecular geometries, particularly in systems with rapidly changing electron densities. One of the GGA functional is the Perdew, Burke, and Ernzerhof (PBE) functional, which is used in this thesis.[49] This functional is widely employed in DFT calculations because it has errors typically within the range of 0.5 eV.

Hybrid GGA

One of the main reasons for the inaccuracy in GGA is self electron interaction. The self-interaction error arises from the method used to compute Hartree energy using the total electron density. In the Kohn-Sham DFT approach, each electron is considered to move within an effective potential generated by all electrons, including itself. This formulation results in each electron erroneously interacting with its own charge distribution when solving the Kohn-Sham equations, thus, introducing self-interaction error. To reduce this self-interaction error hybrid functionals can be used. As the name suggests these are GGA-type functionals combined with some $\sim 25\%$ of the Fock exchange energy from the Hartee-Fock method.[51] The Fock exchange component does not suffer from self-interaction error, thus, improving the description of electron localization, charge transfer, and band gaps.

DFT+U

DFT+U is a simple computational method that addresses the self-interaction error in LDA and GGA functional. The approach is generally used for materials with partially filled d or f orbitals, such as transition metals and rare-earth elements. In DFT+U, the "U" represents the Hubbard U parameter, a correction term that considers the on-site Coulomb interaction among electrons within the same atomic orbital. This corrects the self-interaction errors of DFT and improves the treatment of localized electrons.[52;53] DFT+U is less computationally intensive compared to hybrid functionals, which require the calculation of exact exchange from the Hartree-Fock theory. In this thesis, DFT+U method is used to describe the localized Cu(3d) electrons.

van der Waals interaction

The local (LDA) and semi-local (GGA) exchange-correlation functionals do not include van der Waals interactions, which arise due to long-range interaction of instantaneous dipoles. One of the approaches to effectively describe the vdW interactions is DFT-D3 developed by Grimme and co-workers[54]. This correction adds a pairwise attractive potential decaying with the inverse sixth power of the distance between atoms, typical for van der Waals forces.[55] DFT-D3 is used in this thesis.

2.3.2 Solution of Kohn-Sham equations

Plane wave basis set

The Kohn-Sham orbitals and electron density need to be expanded. Different basis can be used e.g. Gaussians, atomic orbitals, and plane waves.[56] In this work, the Vienna Ab initio Simulation Package (VASP) code has been used[57], which is a plane wave method. Plane waves are nonlocal and span the entire space. Bloch's theorem is a fundamental principle that describes how electrons move in a periodic potential.[58] Additionally, Bloch's theorem plays a crucial role by stating that the wave functions of electrons in a solid can be represented as the product of a plane wave and a function that shares the same periodicity as the crystal lattice.

$$\psi_k(\mathbf{r}) = u_k(\mathbf{r}) \exp(i\mathbf{k} \cdot \mathbf{r}) \tag{2.12}$$

Here $u_k(\mathbf{r})$ is a periodic function that has the same periodicity as the potential such that $u_k(\mathbf{r})u_k(\mathbf{r}) = (\mathbf{r} + \mathbf{R})$.[56]

Pseudopotentials

A significant challenge in electronic structure calculations arises from the different characteristics of electronic wavefunctions in different region of space. Electrons located far from the atomic core typically have smooth wavefunctions, while electrons localized in the core exhibit high-frequency oscillations, complicating the use of plane waves for their representation. To address this issue, pseudopotentials are employed.[59] Pseudopotentials are created to mimic the true potentials of the valence electrons without the need to

account for the core electrons. This is achieved through the process of pseudization, which simplifies the wave functions of valence electrons, making them smoother. Various types of pseudopotentials exist[56], among which the projector augmented wave (PAW)[58] method is used in this thesis. The method involves mapping both core and valence wave functions separately. Valence wave functions (ψ_{inter}) are represented using plane-wave expansions, while core wave functions (ψ_{core}) are projected onto a radial grid centered at the atom. By adding these two components and trimming off the overlapping part (ψ_{net}), the final wave function (ψ_{PAW}) closely resembles the AE wave function.

$$\psi_{\text{PAW}} = \psi_{\text{inter}} + \psi_{\text{core}} - \psi_{\text{net}} \tag{2.13}$$

Solving the Kohn-Sham equation

The potential experienced by the electrons depends on the charge density, see equation 2.6, thus, to achieve self-consistency in the electronic structure calculations, a Self-Consistent Field (SCF) loop is necessary.[47] Initially, the electron densities from each atom in its isolated state are superimposed to construct the starting electron density. Then, U_{xc} and other relevant terms are computed to determine the Kohn-Sham (KS) Hamiltonian. Following this, the set of coupled KS equations is solved to derive the KS orbitals. Using these orbitals, a new electron density is calculated, which includes a mix of the previous densities to refine the approximation. This iterative process continues until the change in energy or density is less than a specified threshold, usually 10^{-4} to 10^{-5} eV, indicating that self-consistency has been reached. At this point, the ground-state energy has been given the nuclear coordinates.

Chapter 3

Calculations of the materials properties

In this chapter, we discuss how computational methodologies can be employed to derive material properties from electronic structure calculations. Specifically, we explore methods for optimizing structures, calculating reaction barriers, and vibrational frequencies. In addition, we will discuss how the change in reaction kinetics can be analyzed.

3.1 Geometry optimization

The most relevant molecular structures are local or global energy minima. The optimization process begins with minimizing the electronic energy at a fixed ionic position. After each electronic relaxation, the force acting on each ion is calculated. The force acting on the nucleus is basically the gradient of the total energy with respect to atomic positions.

$$F_I = -\left(\psi \left| \frac{\partial \hat{H}}{\partial R_I} \right| \psi\right) = \int n(r) \left(\frac{Z_I(r - R_I)}{|r - R_I|^3}\right) d\tau + \sum_{J \neq I} \frac{Z_I Z_J (R_I - R_J)}{|R_I - R_J|^3}, \tag{3.1}$$

Here, the first part of the integral is the electrostatic force on nucleus I due to the charge distribution of the electrons, *n(r)* and the second part of the integral represents the repulsive electrostatic force between nuclei I and J with the charges of the nuclei being Z_I and Z_J, respectively. The forces are calculated using the Hellmann–Feynman theorem,[60;61] which states the forces depend on the Coulomb interaction between the nuclei and the electron density assuming that the Born-Oppenheimer approximation holds. After multiple iterations of minimizing electronic and atomic energies, the system will eventually attain its minimum-energy arrangement, characterized by forces on each atom approaching zero (typically 0.05 eV/Å). There are different methods that can be implemented for minimization: the quasi-Newton method, the conjugate gradient (CG) method, and the damped MD method.[62] In this thesis, the conjugate gradient method has been used.[47] The method begins with an initial geometry, calculates the energy gradient, and uses the energy gradient to set a search direction which is initially the steepest descent. Through line searches, it adjusts atom positions, updating the search direction to be conjugate to previous directions, ensuring efficient convergence. The geometries obtained from these calculations can be compared to experimental data using, for example, diffraction techniques.[63] Sometimes, it can be difficult to locate the global minimum due flat potential energy surface. To obtain lower energy structure in such cases, *ab initio* molecular has been used, which is discussed below.

3.2 Finding transition state and energy barrier

Svante Arrhenius introduced an equation in 1889, proposing a relationship to describe the temperature dependence of the rate constant for an elementary reaction.[64;65] The equation which now is called the Arrhenius equation is:

$$k = Ae^{-\frac{E_a}{k_B T}} \tag{3.2}$$

Here, E_a is the activation energy required for the reactant to be converted into the product. Experimentally, E_a can be determined by plotting the natural logarithm of the rate constant against the inverse temperature (T^{-1}). The slope of this plot provides -E_a/k_B. However, identifying crucial elementary steps in a reaction experimentally can be challenging. and it is important to note that the apparent activation energy in equation 3.2 is an empirical parameter that characterizes how the rate of a reaction responds to changes in temperature. In contrast, the elementary reaction barrier is the actual energy difference between the reactants and the transition state (the highest energy point along the reaction coordinate) for a single reaction step.

One of the widely used methods for finding the transition state is the nudged elastic band method (NEB)[66;67] which is also used in this thesis. To determine the Minimum Energy Path (MEP), a series of images are made between the starting (reactant) and ending states(product). The optimization is such that for each image, only the component of the actual force that is perpendicular to the path is taken into account, while only the parallel component of the spring force is considered. The spring forces then only control the spacing of the images along the band and ensure continuity of the path. The total force acting on the system is a sum of these two (true perpendicular force and parallel spring force), given by:

$$\mathbf{F}_i = \mathbf{F}_i^{\parallel} - \nabla E(\mathbf{R}_i)_{\perp}, \tag{3.3}$$

where the true force is given by

$$\nabla E(\mathbf{R}_i)_{\perp} = \nabla E(\mathbf{R}_i) - (\nabla E(R_i) \cdot \hat{\tau}_i)\,\hat{\tau}_i \tag{3.4}$$

Here, E is the energy of the system, a function of all the atomic coordinates, and $\hat{\tau}_i$ is the normalized local tangent at image i. The spring force is

$$\mathbf{F}_i^{\parallel} = k(|\mathbf{R}_{i+1} - \mathbf{R}_i| - |\mathbf{R}_i - \mathbf{R}_{i-1}|)\hat{\tau}_i, \tag{3.5}$$

where k is the spring constant. An optimization algorithm is used to move the images according to the force. Sometimes, it is possible that the image is not exactly at the saddle point, and for that case we can use the climbing image NEB (CI-NEB)[66] method in which the information about the Minimum Energy Path (MEP) is preserved, while also achieving a precise convergence to a saddle point.

3.3 Vibrational frequency analysis

Vibrational frequencies are essential for various purposes like determining vibrational entropy, zero-point energy, identifying minima, transition states, and molecule-specific

vibrations. These frequencies represent the oscillations of atoms around their equilibrium positions within a system. Calculating the frequencies involves expanding the molecule's energy around its equilibrium position using a Taylor expansion. Given by: [68]

$$E = E_0 + \frac{1}{2}\sum_{i=1}^{3N}\sum_{j=1}^{3N}\left.\frac{\partial^2 E}{\partial x_i \partial x_j}\right|\Delta x_i \Delta x_j \tag{3.6}$$

This approach, which neglects the higher-order terms in the Taylor expansion, is called the harmonic approximation. [56] The first derivative in equation 3.6 is zero because it is at equilibrium. The second term is the second-order partial derivative of the energy E with respect to coordinates x_i and x_j evaluated at the equilibrium position x_0 and multiplied by the product of the displacements Δx_i and Δx_j. If we define

$$H_{ij} = \left[\frac{\partial^2 E}{\partial x_i \partial x_j}\right]_{\mathbf{x}=\mathbf{x}_0} \tag{3.7}$$

then these derivatives define a $3N \times 3N$ matrix known as the Hessian matrix. In vibrational analysis, the law of motion is used to derive the equations that describe the normal modes of vibration. The equations of motion for the system can be expressed in terms of the Hessian matrix and the masses of the atoms, leading to a set of linear equations whose solutions are the vibrational modes. The full set of normal modes in DFT calculations can be calculated by calculating the elements of the Hessian matrix using finite-difference approximations. The $3N$ normal mode frequencies are in this approximation given by the $3N$ eigenvalues of this matrix, $\upsilon_i = \lambda_i/2\pi$ where λ_i is the eigenvalue. Further, having the eigenfrequencies υ_i, the eigenenergies can be obtained by

$$E_{i,n} = h\upsilon_i\left(n + \frac{1}{2}\right), \quad n = 0, 1, 2, \ldots \tag{3.8}$$

where h is the plank's constant. The vibrational frequencies obtained from these calculations can be compared to experiments using infrared spectroscopy (IR).

3.4 Ab initio molecular dynamics

In this thesis, Born-Oppenheimer Ab Initio Molecular Dynamics (AIMD) is employed to explore and identify minimum energy structure of different copper species in CHA in a canonical (NVT) ensemble. The temperature of the simulation is controlled by a Nosé-Hoover thermostat [69;70]

Nosé extended Lagrangian with an extra degree of freedom of heat bath, s:

$$L = \frac{1}{2}\sum_i M_i s^2 v_i^2 - E + \frac{Q}{2}\left(\frac{ds}{dt}\right)^2 - gk_B T\ln(s) \tag{3.9}$$

where the first term is the kinetic energy, the second term is the potential energy. The third and fourth terms represent the kinetic and potential energy of the fictitious coordinates, respectively. Further, Hoover [71] added a friction term to the extended Lagrangian by

introducing a friction coefficient ξ. The temperature of the MD simulation can be controlled by taking the time derivative of this friction coefficient ξ, given by:

$$\frac{d\xi}{dt} = \frac{3Nk_B}{Q}(T_{\mathrm{MD}-T}) \tag{3.10}$$

3.5 Microkinetic modelling

The microkinetic modeling in this thesis is based on the mean-field approach, which assumes that the system is homogeneous and that species are randomly distributed. Moreover, there is no interaction between the adsorbed species. To analyze the kinetics of the reaction, we follow how coverages of the species change with time and temperature. Coverage here means the fraction of each species, which should sum to one. The time evolution of the surface coverages is obtained by solving a set of ordinary differential equations within the framework of a mean-field microkinetic model. [6]

$$\frac{d\theta_j}{dt} = \sum_i v_{ij} r_i \tag{3.11}$$

where θ_j is the fractional coverage of species j, v_{ij} is the stoichiometric coefficient of species j in the elementary reaction i, and r_i is the rate of i-th elementary reaction that depends on the coverages. SciPy is used to numerically solve the differential equations. The solver uses the Backward Differentiation Formula (BDF) method and integrates the differential equations. The coverages obtained can be experimentally compared with the temperature-programmed desorption (TPD).

3.5.1 Adsorption and desorption rate constants

The rate constant for the adsorption of the species i is estimated using collision theory: [6]

$$k_{ads} = \frac{P_i s_0 A}{\sqrt{2\pi m k_B T}} \tag{3.12}$$

where P_i is the pressure of species i, s_0 is the sticking coefficient, A refers to the area of the largest 8-membered ring through which the molecule needs to pass, m is the mass of species i, and k_B is Boltzmann's constant and T is the temperature. Thermodynamic consistency is ensured by calculating the desorption rate constant from k_{ads} and the equilibrium constant:

$$k_{des} = \frac{k_{ads}}{K_{eq}} \tag{3.13}$$

3.5.2 Reaction rate constants

The rate constants for the surface reactions are calculated within the transition state theory. [72] Transition state theory is based on the following assumptions: (1) the product is formed via an activated complex (transition state) through a loose vibration, and (2)

the transition state and the reactants of the elementary steps are in quasi-equilibrium. (3) Species that have passed the transition state from the initial state will immediately form the final state.[73] Hence, for an elementary reaction described by $R_{IS} \rightleftharpoons R_{TS} \rightarrow P$, the rate constant k can is given by

$$k = \nu K \tag{3.14}$$

with ν denoting the crossing frequency at which species at the transition state convert to the final state and K is the equilibrium constant, which can be defined as:

$$K = \frac{Z_{TS}}{Z_{IS}} \tag{3.15}$$

Here, Z_{TS} and Z_{IS} are the partition functions for the transition state and the initial state, respectively. The thermodynamic form of the transition state rate expression is given by:

$$k = \frac{k_B T}{h} \exp(\frac{\Delta S^\dagger}{k_B}) \exp(-\frac{\Delta H^\dagger}{k_B T}) \approx \frac{k_B T}{h} \exp(\frac{\Delta S^\dagger}{k_B}) \exp(-\frac{\Delta E^\dagger}{k_B T}) \tag{3.16}$$

where $\Delta H^\dagger$ and $\Delta S^\dagger$ are the enthalpy and entropy change for the formation of the transition state from the reactants, respectively. As pV does not change along the reaction path, $\Delta H^\dagger$ is approximated by $\Delta E^\dagger$ (the zero-point corrected barrier of the elementary step).

3.5.3 Analysis of reaction kinetics

Order of reaction

One way to characterize a reaction is by examining the dependence of its rate on the concentrations or partial pressures of the reactants, which is expressed in terms of reaction orders. According to rate law, the relationship between the rate and partial pressure of the component is given by[73]:

$$r \propto \prod_i p_i^{n_i} \tag{3.17}$$

The reaction order for a given component i, denoted n_i, can be determined by assessing how the natural logarithm of the rate of the reaction in the forward direction, r^+, changes with respect to the natural logarithm of the component's partial pressure p_i. This relationship is given by[74]:

$$n_i = \frac{\partial \ln r^+}{\partial \ln p_i}, \tag{3.18}$$

Reaction orders are experimentally determined through linear fitting methods. It is important to note that the order of the reaction should be calculated at the rate corresponding to the initial rate. However, the calculation of reaction order is sensitive to temperature, meaning that the reaction order can vary significantly with changes in temperature

Apparent activation energy

In addition to assessing the effect of reactant partial pressures on the reaction rate through reaction orders, one can explore the impact of temperature by examining the apparent activation energy. The apparent activation energy is determined using the Arrhenius equation:

$$r = A \exp\left(-\frac{E_{\text{app}}}{k_B T}\right) \prod_i p_i^{n_i} \tag{3.19}$$

where $\Delta E_{\text{act}}^{\text{app}}$ represents the apparent activation energy, k_B is boltzmann constant, T the temperature, and r^+ the forward reaction rate.[73] This method is similar to the procedure used for finding reaction orders, i.e. it involves a linear fit of the data.

Chapter 4

Experimental

A detailed description of the experimental procedures applied in the thesis is discussed in this chapter. The zeolites have been studied by using flow reactor measurements and temperature-programmed desorption using ammonia.

4.1 Synthesis of the catalyst

The Cu-CHA catalysts were synthesized by impregnating H-CHA zeolite materials (with Si/Al molar ratios of 6.7 and 15) with Cu-nitrate solution. Post-impregnation, the samples underwent a two hours drying period at 90°C, followed by a one-hour calcination at 500°C in air to decompose the nitrates. In this study, 4% CuO/CHA with SAR=13.4 and HCHA with SAR=13.4 were used. An aged catalyst was prepared by exposing the fresh catalyst to 10% of O_2 and 10% of H_2O at 650°C for a specific time which is the standard produre for mild aging condition.

4.2 Temperature-programmed desorption of ammonia

In this thesis, the temperature-programmed reaction (TPR) method is utilized, where a chemical reaction is monitored as the temperature linearly increases over time. Specifically, we employ temperature-programmed desorption (TPD) to analyze the loss of Brønsted acid sites, a key features of the dealumination process in catalysts. The temperature at any given time t during the TPD experiment is given by the equation:

$$T(t) = T_0 + t\beta \tag{4.1}$$

Where $T(t)$ is the temperature at time t, T_0 is the initial temperature, β is the heating rate, which is defined as:

$$\beta = \frac{dT}{dt} \tag{4.2}$$

The rate of desorption can be given as:

$$-\frac{d\Theta}{dt} = k_d\Theta^m \tag{4.3}$$

here, Θ is the surface coverage, m is the order of desorption.

This equation can also be written with respect to temperature:

$$-\frac{d\Theta}{dT} = \frac{k_d\Theta^m}{\beta} \tag{4.4}$$

Having the Arrhenius equation:

$$k_d = A \exp\left(-\frac{E_d}{k_B T}\right) \tag{4.5}$$

and substituting k_d into the equation 4.4, we get the Polanyi-Wigner equation:

$$-\frac{d\Theta}{dT} = \frac{A\Theta^m}{\beta} \exp\left(\frac{-E_d}{k_B T}\right) \tag{4.6}$$

The Polanyi-Wigner equation is a relationship used to describe the kinetics of desorption processes. It states that the rate of desorption is dependent on both the energetic barrier to desorption and the surface coverage.[75] Here, while analyzing the TPD the readsorption of ammonia is considered.

4.2.1 Procedure for ammonia-TPD

NH_3-TPD was conducted in a flow reactor setup. 50 mg of dry catalyst was mixed with 300 mg of SiC to make it homogenous. The experiment took place in a quartz U-tube with a 6 mm diameter, utilizing quartz wool to maintain a fixed catalytic bed reactor.

The procedure involved pre-heating the sample to eliminate any adsorbed species or moisture. Subsequently, at 100°C the sample is exposed to NH_3,assuring NH_3 is adsorbed. The sample was then exposed to water to remove any physisorbed ammonia. Following this, a temperature ramp of 3°C/min from 80°C to 550°C was applied. Chemisorbed ammonia was desorbed at different temperatures from various sites, which were detected and quantified.

4.3 Calculation for rate constant and activity measurement

In mass balance calculations, the conservation of mass is the foundational principle, summarized by the equation:

$$\text{Inlet} - \text{Outlet} + \text{Generation} = \text{Accumulation}$$

This equation indicates that the mass entering a system, minus the mass exiting, plus any generated mass, equals the mass accumulated over time. In a steady-state process, where there is no accumulation, the equation simplifies to:

$$n_{\mathrm{A(in)}} - n_{\mathrm{A(out)}} + r\Delta W = 0$$

$\mathrm{n_{A(in)}}$ and $\mathrm{n_{A(out)}}$ are the moles of species A coming in and out of the system, respectively. r is the rate of generation. ΔW is the change in weight or volume due to reaction (weight in our case). The moles can be written as flow multiplied by concentration. The mass balance equation can be written as:

$$F_{\mathrm{in}} C_{\mathrm{A,in}} - F_{\mathrm{out}} C_{\mathrm{A,out}} + r_A \Delta W = 0$$

where F is the flow rate, C_A is the concentration of species A.

If the flow is kept constant, then the equation simplifies assuming no change in flow rate. For ammonia SCR, there is a little bit of expansion going from reactants to products, but the concentration is so low that it cannot be measured. This simplifies further:

$$F(dC) + r_A \Delta W = 0$$

$$\frac{dC}{dW/F} = -r_A$$

Defining conversion, X, as the ratio of the change in concentration to the initial concentration:

$$X = \frac{C_{A_0} - C_A}{C_{A_0}}$$

where C_{A0} is the initial concentration and C_A is the final concentration. The rate of reaction, considering a first-order reaction, is:

$$r_A = kC_A$$

Substituting and rearranging, we derive the fundamental relationship:

$$\frac{C_{A_0} dX}{dW/F} = r_A$$

Assuming no change in flow rate, the kinetics are simplified, leading to:

$$\frac{dX}{1 - X} = kd\tau$$

where τ represents the contact time. Integrating and applying boundary conditions, we get the solution for X:

$$X = 1 - e^{-k\tau}$$

This relationship is crucial for understanding the progression of conversion over time in a first-order reaction, providing a pathway to evaluate the rate constant k by the expression:

$$-\frac{\ln(1 - X)}{\tau} = k$$

This formula is essential for determining the kinetics of the reaction and can be further used to calculate the apparent activation energy from the plot $\ln(k)$ versus $1/T$.[76]

In this thesis, we investigate the rate constant and activation energy to analyze the NH_3-SCR reaction. The NO_x conversion and the space velocity (W/F) are determined, and the rate constant, k, for the SCR reaction is derived using the formula:

$$\mathrm{k} = -\ln(1 - \mathrm{X}_{NO})/(W/F)$$

This formula is based on the assumption that the NH_3-SCR reaction follows first-order kinetics with respect to NO_x concentration.

4.3.1 Procedure for rate constant and activity measurement

The Cu-CHA sample was prepared in a similar way as for ammonia TPD. Depending on the copper loading, the activity measurements were done at different temperatures to ensure NO_x conversion is lower than 80%. This is done to accurately determine the rate constant k, it is crucial to take measurements from the portion of the curve where there is a noticeable slope. This is because the slope represents the rate of change, which is essential for calculating k. Measurements taken from the flat part of the curve, where the rate of change is zero, would not provide meaningful data for this analysis.

Prior to the measurements, the sample is degreened by heating at 500 °C in 10% O_2 for 30 minutes. The activity measurement are performed with 500 ppm of NO, 600 ppm of NH_3, 10% O_2, and different partial pressure of water with an N_2 balance.

Chapter 5

Results

5.1 Introduction

It is important to study the interaction of water with the copper sites and the zeolite framework as diesel engine exhaust streams typically contain 2-9% water. In this thesis, the interaction is studied at both low and high temperatures. At lower temperatures, water's impact is confined to adsorption onto various sites within the zeolite structure and Cu-species. However, at high temperatures, water adsorption can result in dealumination, which leads to deactivation of the catalyst.

The influence of water at low temperatures was explored in **Paper II**. We examined experimentally how changes in temperature and water partial pressure affect the NH_3-SCR reaction. DFT calculations were employed to elucidate how water blocks different sites that are part of the NH_3-SCR reaction cycle. These results were then integrated into the microkinetic model to understand the details of the kinetics.

Further, at high temperatures, we discuss the mechanism of dealumination in H-CHA and Cu-CHA in **Paper I**. The presence of Cu has been measured to reduce the rate of dealumination, thus, stabilizing the catalyst. [36] To understand the kinetics of dealumination in both H-CHA and Cu-CHA, a microkinetic model was developed. Additionally, the model was used to investigate the impact of aluminum distribution, aligning the findings with experimental results.

5.2 Effects of water on the low-temperature NH_3-SCR

5.2.1 Experimental results

Figure 5.1(A) presents NO_x conversion at various temperatures under dry and wet conditions, demonstrating that increase in NO_x conversion with temperature up to 260°C. The addition of water significantly reduces NO_x conversion, indicative of its inhibitory effects at low temperatures. Figure 5.1 (B) extends this analysis across water pressures ranging from 0% to 20%, confirming the trend of decreased NO_x conversion beyond 2% water presence.

The rate constant for the reaction is calculated for pressures ranging from 0% to 20% and analyzed $\ln(k')$ as a function of $\ln(p_{H_2O})$ in Figure 5.1 (C). The analysis shows how water influences the kinetic rate constant, with a decreasing rate as water partial pressure increases. The decrease in constant with increasing water partial pressure is fitted using an exponential decay function $f(x) = a\,e^{bx} + c$ with the fitted parameters a = -6.98, b = 1.01, c = 4.77 and an R^2 value of 0.971.

The slope of $\ln(k')$ against $\ln(p_{H_2O})$ gives the reaction order of water as a function of water partial pressure. The reaction order is calculated as the derivative of the fitted exponential decay function, which is given by $a\,b\,e^{bx}$ as shown in Figure 5.1 (D). The reaction order shows a linear dependence on (p_{H_2O}). The reaction order changes from -0.11 to -1.38 with increasing water concentration from 1.74% to 20%. The variation reveals that the inhibition is pronounced at high pressures where water acts as a poison for the reaction.

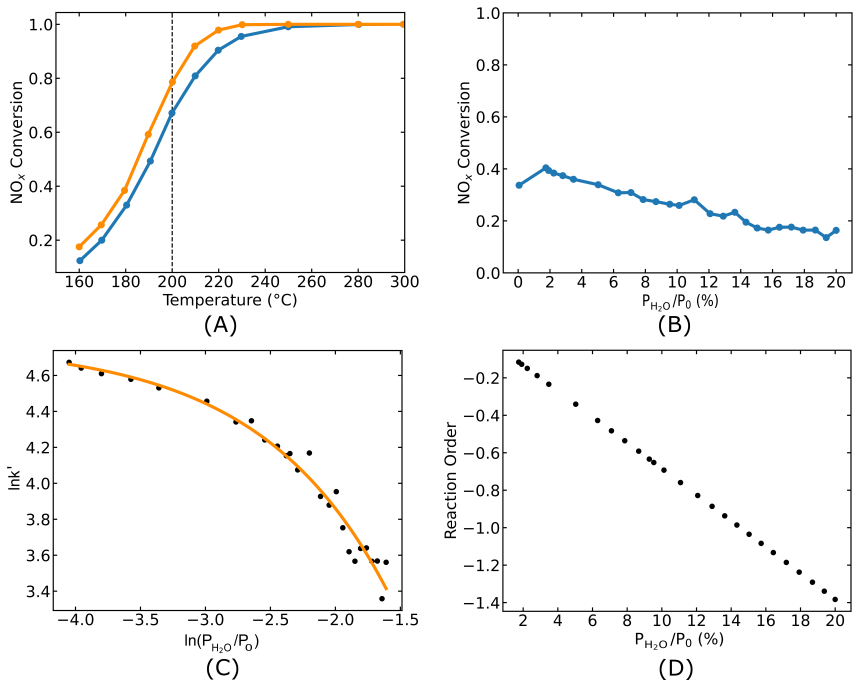

Figure 5.1: NO_x conversion over 4% CuO/CHA SAR = 13.4 (A) at different temperatures and (B) at different pressures. (C) Natural logarithm of the rate constant ($\ln(k')$) as a function of the natural logarithm of water partial pressure ($\ln(P_{H_2O}/P^0)$). The solid line is a fit to the experimental data. (D) Shows the reaction order in H_2O as a function of the partial pressure of H_2O. Reaction conditions (A): 10% O_2, 500 ppm NO, 600 ppm NH_3, 5% H_2O in wet condition. Reaction conditions (B), (C), (D): 200 °C, 10% O_2, 500 ppm NO, and 600 ppm NH_3.

5.2.2 DFT calculations

According to the proposed reaction cycles[77] (Figure 5.2), the NH_3-SCR process starts with the adsorption of O_2 onto $[Cu(NH_3)_2]^+$ pairs, resulting in the formation of Cu-peroxo species, $[Cu_2(NH_3)_4O_2]^{2+}$. Subsequently, NH_3 and NO react with the Cu-peroxo species,

leading to the formation of H_2NNO and the $[Cu_2(NH_3)_4OHOH]^{2+}$ complex. The H_2NNO intermediate then migrates to a Brønsted acid site, where it undergoes decomposition into N_2 and H_2O, facilitated by ammonium (NH_4^+). The microkinetic model based on

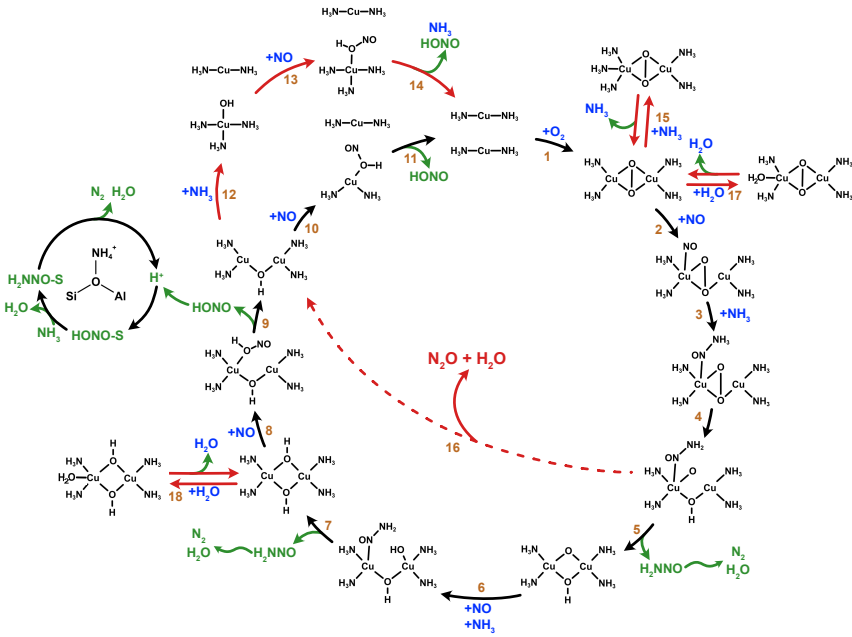

Figure 5.2: Proposed reaction Cycle for low-temperature NH_3-SCR over Cu-CHA with water adsorption on $[Cu_2(NH_3)_4O_2]^{2+}$ and $[Cu_2(NH_3)_4(OH)_2]^{2+}$. According to the reference [77;78]

the proposed reaction cycle shows that the peroxo complexes and $[Cu_2(NH_3)_4OHOH]^{2+}$ intermediates are the dominant coverages at low temperatures, particularly around 200 °C[77;78]. Density Functional Theory (DFT) calculations were performed on the chabazite structure using a rhombohedral unit cell that consists of 12 Si atoms in tetrahedral(T) positions. In our case, we replace 2 Si atoms with Al, resulting in a Si/Al ratio of 5. The calculations showed that water molecules competitively adsorb on these sites, impacting the reaction cycle. Specifically, a water molecule on the Cu site of the Cu-peroxo complex exhibits an adsorption energy of 0.79 eV, higher than the 0.70 eV for NO, indicating a competitive reaction. A second water molecule can also adsorb on the second Cu site with an energy of 0.62 eV. Similarly, water on the $[Cu_2(NH_3)_4OHOH]^{2+}$ intermediate adsorbs with an energy of 0.66 eV, surpassing NO's adsorption energy (0.25 eV), thereby hindering this step. Figure 5.4 shows the adsorption of water on the Cu-peroxo and $[Cu_2(NH_3)_4OHOH]^{2+}$ intermediate. However, water does not affect the formation of $[Cu(NH_3)_2]^{+1}$ or the ammonia exchange by water in the peroxo complex.

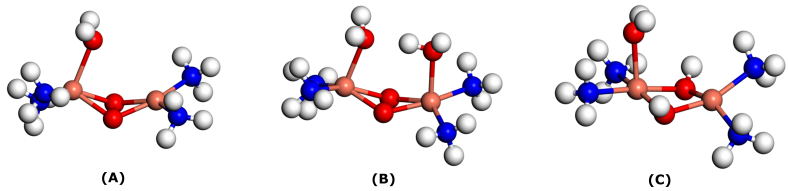

Figure 5.3: Structure of (a) one water adsorbed peroxo complex, (b) two water molecules adsorbed peroxo complex, and (c) (a) one water adsorbed $[Cu_2(NH_3)_4OHOH]^{2+}$ complex. Atomic color codes: Cu (bronze), Si (yellow), O (red), and H (white).

5.2.3 Microkinetic model

A DFT-based microkinetic model that considered the blocking of active sites by water, the desorption of water was initially constructed using a Gibbs free energy equation incorporating enthalpy (ΔH), entropy ($T\Delta S$) with the normal $\log(P/P_0)$ dependence in entropy . However, this initial model did not align well with experimental data. To resolve this, the model was refined by modifying the desorption energy to include water concentration effects through an additional pressure term (0.169 * P) in the enthalpy. Thus, the enthalpy is given by: $\Delta H = \Delta H_0 + 0.169 * P$ (in eV). The improved model was able to reproduce the observed changes in reaction order with respect to water pressure.

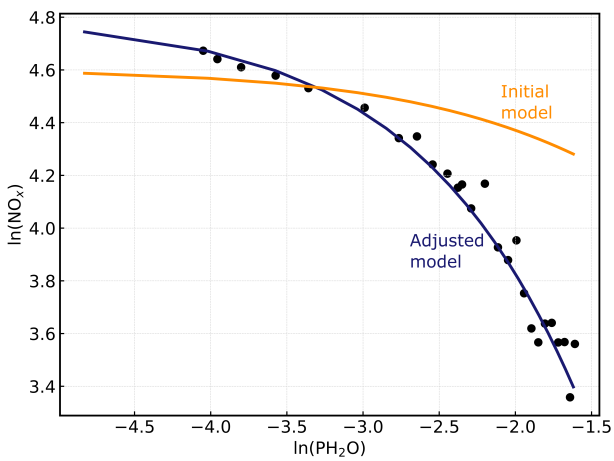

Figure 5.4: Simulated and experimental reaction order versus the pressure of H_2O. The simulations are performed at 200 °C with 600 ppm NH_3, 500 ppm NO and 10% O_2

5.3 Dealumination mechanism

For H-CHA, the dealumination has been suggested to occur in four consecutive steps to result in the formation of extra framework aluminum (as $Al(OH)_3H_2O$).[79] In each step, a single Al-O bond in the zeolite is hydrolyzed to the corresponding Al-OH and Si-OH in the framework. The highest energy barrier is 0.85 eV, corresponding to the hydrolysis of the first Al-O bond.

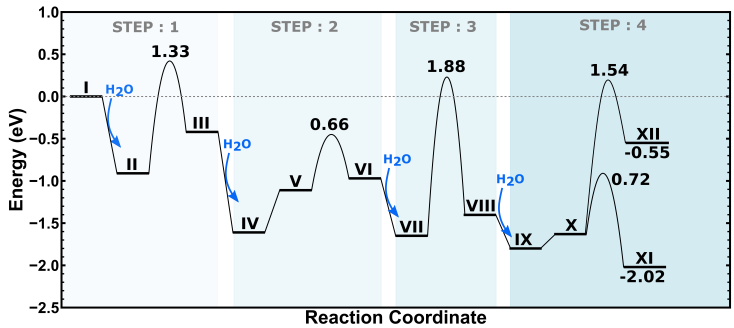

Figure 5.5: Potential energy landscape for dealumination of Cu-CHA.

A similar reaction path was considered for dealumination in Cu-CHA. Figure 5.5 illustrates the energy landscape for Cu-CHA's dealumination process with the corresponding structures in Figure 5.6. Cu-CHA follows a similar reaction path with four consecutive hydrolysis steps. However, in this case, it can result in the formation of two products, either $Al(OH)_3H_2O$ or a Cu-Al species, $Cu(OH)_2Al(OH)(H_2O)$. The highest energy barrier in this case is 1.80 eV, and occurs at the hydrolysis of the third Al-O bond. The higher barrier indicates that the Cu-ion stabilizes the CHA structure of the zeolite. Additionally, the preferred reaction product after complete dealumination of Cu-CHA is a Cu-Aluminate-like species bound to the zeolite framework.

5.4 Effect of aluminum distribution on dealumination in H-CHA

The rate of dealumination in H-CHA zeolites is primarily influenced by the first hydrolysis barrier. The dependence of this barrier on the Al-distribution was studied in detail. Calculations for eight different Al configurations revealed that the lowest energy barrier of 0.85 eV occurs when Al atoms are on opposite sides of a six-membered ring. Configurations with Al atoms in adjacent six- and eight-membered rings result in higher barriers, up to 1.23 eV. Figure 5.7 shows the kinetics of extra-framework aluminum (EFAL) formation at 923 K, showing a pronounced delay in EFAL formation for the highest barrier, demonstrating that Al distribution is a critical factor in the dealumination process.

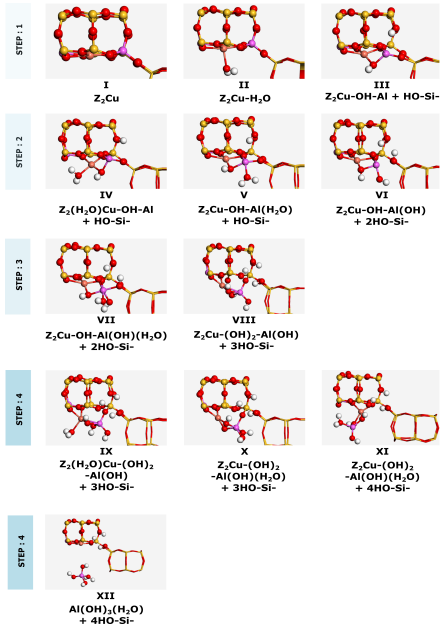

Figure 5.6: Intermediates for dealumination of Cu-CHA. Atomic color codes: Atomic color codes: Cu (bronze), Si (yellow), Al (pink), O (red), and H (white).

5.5 Linking microkinetic model to the experimental results

The effect of Al distribution on dealumination can be experimentally verified with the help of ammonia temperature-programmed desorption. The loss of Brønsted acid sites is one of the key features of the dealumination process. This can be effectively analyzed using temperature-programmed desorption (TPD). Figure 5.8 presents the TPD profiles of both fresh and aged H-CHA. Aging was achieved by exposing the fresh catalyst to 10% of O_2 and 10% of H_2O at 650°C for defined duration. Fresh H-CHA displays a single and high-intensity peak, indicating a significant amount of Brønsted acid sites that desorbs ammonia. However, the notable amount of ammonia released after just one hour of aging suggests that H-CHA experiences significant dealumination early on. As aging progresses beyond an hour, the decrease in the peak intensity slows down, suggesting a two-stage deactivation: fast deactivation resulting from loss of Brønsted acid sites within the first hour, followed by a slow deactivation which can result from loss of Brønsted acid sites different distribution of Al over a longer duration up to 100 hours. In addition to this, the shift in the peak to the left is observed which suggests the nature of the sites might be changing, possibly due to dealumination that makes the sites less effective at binding NH_3.

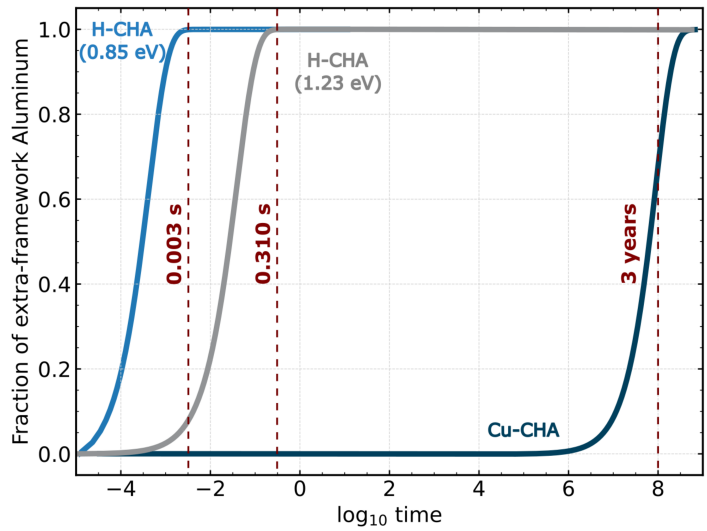

Figure 5.7: Coverage of the extra-framework aluminum species (EFALs) as a function of time at 923 K for H-CHA (low barrier and high barrier shown with blue and grey lines respectively) and Cu-CHA (shown in red).

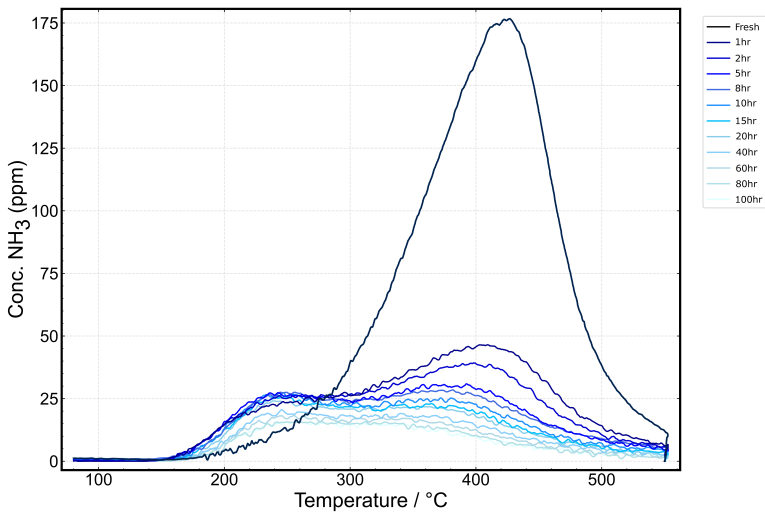

Figure 5.8: TPD profile depicts the desorption of ammonia over H-CHA with SAR 13.4.

Chapter 6

Conclusions and outlook

The main objective of this thesis has been to get an understanding how water influences the activity of Cu-CHA catalysts for NH_3-SCR at low temperatures and hydrothermal stability of Cu-CHA at high temperatures. This has been done by investigating the interaction of the water with various intermediates. The used methodology is based on first-principles calculations using density functional theory (DFT), combined with mean-field microkinetic modeling and experiments.

Several steps were taken to understand the influence of water. Initially, NO_x conversion as a function of temperature and partial pressure of water under both dry and wet conditions was measured. It was observed that the NO_x conversion decreased in the presence of water at temperatures below 260°C and after a water partial pressure of 2% (at 200°C). Furthermore, this effect was quantitatively captured in the reaction order, which shifts from 0 in the absence of the water to-1.4 at 20% H_2O.

The experiments were corroborated by the NH_3-SCR reaction cycle analysis, which identifies the competitive adsorption of water molecules on the active sites of the catalytic process as a primary inhibitory mechanism. Specifically, DFT calculations reveal that water molecules adsorb more strongly than NO on the Cu sites of $[Cu_2(NH_3)_4O_2]^{2+}$ and $[Cu_2(NH_3)_4OHOH]^{2+}$ complexes. A DFT-based microkinetic model fitted with the experimental data when the effect of water desorption energy was included.

Water interacts with zeolite at high temperatures, leading to the removal of Al from the framework, a process known as dealumination. In comparing Cu-CHA and H-CHA under the same conditions, it was observed that Cu-CHA undergoes less dealumination. This delay in dealumination in Cu-CHA was investigated using density functional theory calculations in combination with ab initio thermodynamics and microkinetic modeling. It was discovered that introducing copper into the zeolite structure increases the barriers for dealumination compared to H-CHA, thus, decreasing the rate of dealumination in the presence of Cu. With Cu, some of the extra-framework Al species in the zeolite form bonds with the copper ions, resulting in Cu-bound Al species. This formation is thermodynamically favorable compared to the formation of $Al(OH)_3H_2O$ species. Additionally, the reversibility of the formation of Cu-bound Al species contributes to the decreased rate of dealumination in the presence of Cu.

Further analysis showed that the formation of Al_2O_3 or Al_2O_3 + CuO is thermodynamically preferred with respect to the formation of extra-framework aluminum at high temperatures. The microkinetic model showed a clear temperature difference in the onset of dealumination for H-CHA and Cu-CHA. In the case of H-CHA, the barrier for the first hydrolysis step was calculated for different Al-distributions. The Al-distribution was found to clearly affect the barrier, with a difference of ∼0.4 eV between the lowest and highest barrier.

6.1 Outlook

By investigating the mechanism of dealumination in Cu-CHA in combination with a microkinetic model makes it possible to understand the kinetics of the reaction. However, the kinetic of the reaction with experimental validation using methods such as temperature-programmed desorption has not been studied. As a next step, we would like to explore the reaction kinetics for different Cu/Al ratios and different SAR.

While the loss of Bronsted acid sites within the initial two hours of aging is observed experimentally, the catalyst continues to exhibit activity. This indicates the possibility to decompose HONO and H_2NNO over other sites than Bronsted acid sites. Therefore, work is needed to explore the reaction mechanism over alternative sites,such as silanol groups.

Acknowledgments

The research was carried out at the Division of Chemical Physics and Competence Centre for Catalysis at Chalmers University of Technology, Göteborg, Sweden and at Umicore Denmark ApS, Hørsholm, Denmark in the period February 2022 to April 2024.

The research is funded by the European Union's Horizon 2020 research and innovation program under the Marie Sklodowska-Curie grant agreement no 955839 (CHASS).

The Competence Centre for Catalysis is hosted by Chalmers University of Technology, and financially supported by the Swedish Energy Agency, and the member companies: AB Volvo, ECAPS AB, Johnson Matthey AB, Preem AB, Scania CV AB, and Umicore Denmark Aps.

Computational time was granted by NAISS at NSC (Linköping) and PDC (Stockholm).

In addition I would like to thank:

My main supervisors, Henrik Grönbeck and Ton V. W. Janssens. Thank you for your guidance, support, and patience. I greatly appreciate your availability for discussions and the time you dedicate to our regular meetings.

My co-supervisor, Anders Hellman, and examiner Magnus Skoglundh, for your discussion and advice.

All the members of the CHASS project, for the discussions and encouragement at all the presentations.

All my colleagues at Chemical Physics, KCK, and Umicore are gratefully acknowledged. Thank you for creating a nice and friendly working environment.

All my friends, especially Rahul, Ankita, and Prathistha, for all the support, care, and fun moments.

And of course my parents, and brother for your encouragement, support, and love throughout my life.

Bibliography

[1] Twigg, M. V. Progress and future challenges in controlling automotive exhaust gas emissions. *Applied Catalysis B: Environmental*, *70* (2007), 2–15.

[2] Casper, J. K. *Fossil fuels and pollution: the future of air quality*. Infobase Publishing, 2010.

[3] Johnson, T. V. Diesel emission control in review. *SAE Transactions*, (2001), 128–144.

[4] Granger, P. and Parvulescu, V. I. Catalytic NO x abatement systems for mobile sources: from three-way to lean burn after-treatment technologies. *Chemical Reviews*, *111* (2011), 3155–3207.

[5] Nova, I. and Tronconi, E. *Urea-SCR Technology for DeNO$_x$ After Treatment of Diesel Exhausts*. Springer Science+Business Media New York, 2014.

[6] Chorkendorff, I. and Niemantsverdriet, J. W. *Concepts of modern catalysis and kinetics*. John Wiley & Sons, 2017.

[7] Smith, J. K. History of catalysis. *Encyclopedia of catalysis*, (2002).

[8] Dumesic, J. A.; Huber, G. W.; and Boudart, M. Principles of Heterogeneous Catalysis. In Handbook of Heterogeneous Catalysis. (2008), 1–26.

[9] Sun, Q.; Gao, Z.-X.; Chen, H.-Y.; and Sachtler, W. M. Reduction of NOx with ammonia over Fe/MFI: reaction mechanism based on isotopic labeling. *Journal of Catalysis*, *201* (2001), 89–99.

[10] Brandenberger, S.; Kröcher, O.; Tissler, A.; and Althoff, R. The state of the art in selective catalytic reduction of NOx by ammonia using metal-exchanged zeolite catalysts. *Catalysis Reviews*, *50* (2008), 492–531.

[11] Zhang, D. and Yang, R. T. N2O formation pathways over zeolite-supported Cu and Fe catalysts in NH3-SCR. *Energy & fuels*, *32* (2018), 2170–2182.

[12] Gonzales, R. H. *Diesel exhaust emission system temperature test*. US Department of Agriculture, 2008.

[13] Bauerie, G.; Wu, S.; and Nobe, K. Reduction of nitric oxide with ammonia on noble metal catalysts. *Industrial & Engineering Chemistry Product Research and Development*, *14* (1975), 123–130.

[14] Inomata, M.; Miyamoto, A.; and Murakami, Y. Mechanism of the reaction of NO and NH3 on vanadium oxide catalyst in the presence of oxygen under the dilute gas condition. *Journal of Catalysis*, *62* (1980), 140–148.

[15] Kato, A.; Matsuda, S.; Nakajima, F.; Imanari, M.; and Watanabe, Y. Reduction of nitric oxide with ammonia on iron oxide-titanium oxide catalyst. *The Journal of Physical Chemistry*, *85* (1981), 1710–1713.

[16] Williamson, W. B. and Lunsford, J. H. Nitric oxide reduction with ammonia over copper (II) Y zeolites. *The Journal of Physical Chemistry*, *80* (1976), 2664–2671.

[17] Seiyama, T.; Arakawa, T.; Matsuda, T.; Takita, Y.; and Yamazoe, N. Catalytic activity of transition metal ion exchanged Y zeolites in the reduction of nitric oxide with ammonia. *Journal of Catalysis*, *48* (1977), 1–7.

[18] Jansson, J. Vanadia-based catalysts for mobile SCR. In *Urea-SCR technology for deNOx after treatment of diesel exhausts*, pages 65–96. Springer, 2014.

[19] Chen, H.; Xia, Y.; Fang, R.; Huang, H.; Gan, Y.; Liang, C.; Zhang, J.; Zhang, W.; and Liu, X. The effects of tungsten and hydrothermal aging in promoting NH3-SCR activity on V2O5/WO3-TiO2 catalysts. *Applied Surface Science*, *459* (2018), 639–646.

[20] Hoelderich, W.; Sanati, M.; and Spivey, J. *Catalysis*. Royal Society of Chemistry, 2002.

[21] Ye, B.; Jeong, B.; Lee, M.-j.; Kim, T. H.; Park, S.-S.; Jung, J.; Lee, S.; and Kim, H.-D. Recent trends in vanadium-based SCR catalysts for NOx reduction in industrial applications: stationary sources. *Nano Convergence*, *9* (2022), 51.

[22] Čejka, J.; Morris, R.; and Nachtigall, P. *Zeolites in Catalysis: Properties and Applications*. Royal Society of Chemistry, 2017.

[23] Davis, M. E. Ordered porous materials for emerging applications. *Nature*, *417* (2002), 813–821.

[24] Davis, M. E. and Lobo, R. F. Zeolite and molecular sieve synthesis. *Chemistry of Materials*, *4* (1992), 756–768.

[25] Xin, Y.; Li, Q.; and Zhang, Z. Zeolitic materials for DeNOx selective catalytic reduction. *ChemCatChem*, *10* (2018), 29–41.

[26] Beale, A. M.; Gao, F.; Lezcano-Gonzalez, I.; Peden, C. H.; and Szanyi, J. Recent advances in automotive catalysis for NO x emission control by small-pore microporous materials. *Chemical Society Reviews*, *44* (2015), 7371–7405.

[27] Mohan, S.; Dinesha, P.; and Kumar, S. NOx reduction behaviour in copper zeolite catalysts for ammonia SCR systems: A review. *Chemical Engineering Journal*, *384* (2020), 123253.

[28] Kwak, J. H.; Tran, D.; Burton, S. D.; Szanyi, J.; Lee, J. H.; and Peden, C. H. Effects of hydrothermal aging on NH3-SCR reaction over Cu/zeolites. *Journal of Catalysis*, *287* (2012), 203–209.

[29] Kwak, J. H.; Tonkyn, R. G.; Kim, D. H.; Szanyi, J.; and Peden, C. H. Excellent activity and selectivity of Cu-SSZ-13 in the selective catalytic reduction of NOx with NH3. *Journal of Catalysis*, *275* (2010), 187–190.

[30] Gao, F. and Szanyi, J. On the hydrothermal stability of Cu/SSZ-13 SCR catalysts. *Applied Catalysis A: General*, *560* (2018), 185–194.

[31] Sano, T.; Ikeya, H.; Kasuno, T.; Wang, Z.; Kawakami, Y.; and Soga, K. Influence of crystallinity of HZSM-5 zeolite on its dealumination rate. *Zeolites*, *19* (1997), 80–86.

[32] Luo, J.; Gao, F.; Kamasamudram, K.; Currier, N.; Peden, C. H.; and Yezerets, A. New insights into Cu/SSZ-13 SCR catalyst acidity. Part I: Nature of acidic sites probed by NH3 titration. *Journal of Catalysis*, *348* (2017), 291–299.

[33] Campbell, S. M.; Bibby, D. M.; Coddington, J. M.; Howe, R. F.; and Meinhold, R. H. Dealumination of HZSM-5 zeolites: I. Calcination and hydrothermal treatment. *Journal of Catalysis*, *161* (1996), 338–349.

[34] Masuda, T.; Fujikata, Y.; Mukai, S. R.; and Hashimoto, K. Changes in catalytic activity of MFI-type zeolites caused by dealumination in a steam atmosphere. *Applied Catalysis A: General*, *172* (1998), 73–83.

[35] Fickel, D. W.; D'Addio, E.; Lauterbach, J. A.; and Lobo, R. F. The ammonia selective catalytic reduction activity of copper-exchanged small-pore zeolites. *Applied Catalysis B: Environmental*, *102* (2011), 441–448.

[36] Fickel, D. W. and Lobo, R. F. Copper coordination in Cu-SSZ-13 and Cu-SSZ-16 investigated by variable-temperature XRD. *The Journal of Physical Chemistry C*, *114* (2010), 1633–1640.

[37] Han, S.; Cheng, J.; Zheng, C.; Ye, Q.; Cheng, S.; Kang, T.; and Dai, H. Effect of Si/Al ratio on catalytic performance of hydrothermally aged Cu-SSZ-13 for the NH3-SCR of NO in simulated diesel exhaust. *Applied Surface Science*, *419* (2017), 382–392.

[38] Schrödinger, E. Quantisierung als eigenwertproblem. *Annalen der physik*, *385* (1926), 437–490.

[39] Born, M. and Oppenheimer, R. On the quantum theory of molecules. In *Quantum Chemistry: Classic Scientific Papers*, pages 1–24. World Scientific, 2000.

[40] Hartree, D. R. The wave mechanics of an atom with a non-Coulomb central field. Part I. Theory and methods. In *Mathematical Proceedings of the Cambridge Philosophical Society*, volume 24, pages 89–110. Cambridge university press, 1928.

[41] Fock, V. Näherungsmethode zur Lösung des quantenmechanischen Mehrkörperproblems. *Zeitschrift für Physik*, *61* (1930), 126–148.

[42] Thomas, L. H. The calculation of atomic fields. In *Mathematical proceedings of the Cambridge philosophical society*, volume 23, pages 542–548. Cambridge University Press, 1927.

[43] Fermi, E. Statistical method to determine some properties of atoms. *Rend. Accad. Naz. Lincei*, *6* (1927), 5.

[44] Hohenberg, P. and Kohn, W. Inhomogeneous Electron Gas. *Physical Review*, *136* (1964), B864–B871.

[45] Kohn, W. and Sham, L. J. Self-consistent equations including exchange and correlation effects. *Physical review*, *140* (1965), A1133.

[46] Sousa, S. F.; Fernandes, P. A.; and Ramos, M. J. General performance of density functionals. *The Journal of Physical Chemistry A*, *111* (2007), 10439–10452.

[47] Lee, J. G. *Computational materials science: an introduction.* CRC press, 2016.

[48] Ceperley, D. M. and Alder, B. J. Ground State of the Electron Gas by a Stochastic Method. *Physical Review Letter*, *45* (1980), 566–569.

[49] Perdew, J. P.; Burke, K.; and Ernzerhof, M. Generalized gradient approximation made simple. *Physical Review Letters*, *77* (1996), 3865.

[50] Perdew, J. P.; Chevary, J. A.; Vosko, S. H.; Jackson, K. A.; Pederson, M. R.; Singh, D. J.; and Fiolhais, C. Atoms, molecules, solids, and surfaces: Applications of the generalized gradient approximation for exchange and correlation. *Physical review B*, *46* (1992), 6671.

[51] Kurth, S.; Perdew, J. P.; and Blaha, P. Molecular and solid-state tests of density functional approximations: LSD, GGAs, and meta-GGAs. *International Journal of Quantum Chemistry*, *75* (1999), 889–909.

[52] Anisimov, V. I.; Zaanen, J.; and Andersen, O. K. Band theory and Mott insulators: Hubbard U instead of Stoner I. *Physical Review B*, *44* (1991), 943.

[53] Himmetoglu, B.; Floris, A.; De Gironcoli, S.; and Cococcioni, M. Hubbard-corrected DFT energy functionals: The LDA+ U description of correlated systems. *International Journal of Quantum Chemistry*, *114* (2014), 14–49.

[54] Grimme, S.; Antony, J.; Ehrlich, S.; and Krieg, H. A consistent and accurate ab initio parametrization of density functional dispersion correction (DFT-D) for the 94 elements H-Pu. *The Journal of Chemical Physics*, *132* (2010).

[55] Grimme, S. Semiempirical GGA-type density functional constructed with a long-range dispersion correction. *Journal of Computational Chemistry*, *27* (2006), 1787–1799.

[56] Sholl, D. S. and Steckel, J. A. *Density functional theory: a practical introduction.* John Wiley & Sons, 2022.

[57] Kresse, G. and Furthmüller, J. Efficient iterative schemes for ab initio total-energy calculations using a plane-wave basis set. *Physical review B*, *54* (1996), 11169.

[58] Blöchl, P. E. Projector augmented-wave method. *Physical Review B*, *50* (1994), 17953.

[59] Heine, V. The pseudopotential concept. *Solid state physics*, *24* (1970), 1–36.

[60] Hellman, H. Einführung in die Quantenchemie. *Franz Deuticke, Leipzig*, *285* (1937), 90.

[61] Feynman, R. P. Forces in molecules. *Physical Review*, *56* (1939), 340.

[62] Martin, R. M. *Electronic structure: basic theory and practical methods*. Cambridge university press, 2020.

[63] Xi, Y.; Su, C.; Ottinger, N. A.; and Liu, Z. G. Effects of hydrothermal aging on the sulfur poisoning of a Cu-SSZ-13 SCR catalyst. *Applied Catalysis B: Environmental*, *284* (2021), 119749.

[64] Arrhenius, S. Üon the reaction rate during the inversion of cane sugar by acids. *Journal for Physical Chemistry*, *4* (1889), 226–248.

[65] Logan, S. The origin and status of the Arrhenius equation. *Journal of Chemical Education*, *59* (1982), 279.

[66] Henkelman, G.; Uberuaga, B. P.; and Jónsson, H. A climbing image nudged elastic band method for finding saddle points and minimum energy paths. *The Journal of Chemical Physics*, *113* (2000), 9901–9904.

[67] Henkelman, G. and Jónsson, H. Improved tangent estimate in the nudged elastic band method for finding minimum energy paths and saddle points. *The Journal of Chemical Physics*, *113* (2000), 9978–9985.

[68] Baker, J. Molecular structure and vibrational spectra. *Handbook of Computational Chemistry*, (2012), 423–496.

[69] Nosé, S. A unified formulation of the constant temperature molecular dynamics methods. *The Journal of Chemical Physics*, *81* (1984), 511–519.

[70] Nosé, S. A molecular dynamics method for simulations in the canonical ensemble. *Molecular physics*, *52* (1984), 255–268.

[71] Hoover, W. G. Canonical dynamics: Equilibrium phase-space distributions. *Physical Review A*, *31* (1985), 1695.

[72] Eyring, H. The activated complex and the absolute rate of chemical reactions. *Chemical Reviews*, *17* (1935), 65–77.

[73] Filot, I. *Introduction to microkinetic modeling*. Technische Universiteit Eindhoven, December 2018. ISBN 978-90-386-4520-9.

[74] Motagamwala, A. H. and Dumesic, J. A. Microkinetic modeling: a tool for rational catalyst design. *Chemical Reviews*, *121* (2020), 1049–1076.

[75] Schroeder, S. L. and Gottfried, M. Temperature-programmed desorption (TPD) thermal desorption spectroscopy (TDS). *Adv. Phys. Chem. Lab, FU Berlin*, (2002), 1–22.

[76] Levenspiel, O. *Chemical Reaction Engineering*. John wiley & sons, 1998.

[77] Chen, L.; Janssens, T. V.; Vennestrøm, P. N.; Jansson, J.; Skoglundh, M.; and Grönbeck, H. A complete multisite reaction mechanism for low-temperature NH3-SCR over Cu-CHA. *ACS Catalysis*, *10* (2020), 5646–5656.

[78] Feng, Y.; Wang, X.; Janssens, T. V.; Vennestrøm, P. N.; Jansson, J.; Skoglundh, M.; and Grönbeck, H. First-principles microkinetic model for low-temperature NH3-assisted selective catalytic reduction of NO over Cu-CHA. *ACS Catalysis*, *11* (2021), 14395–14407.

[79] Silaghi, M.-C.; Chizallet, C.; Sauer, J.; and Raybaud, P. Dealumination mechanisms of zeolites and extra-framework aluminum confinement. *Journal of Catalysis*, *339* (2016), 242–255.